



HAL
open science

Velocity Adjustment in Surface Hopping: Ethylene as a Case Study of the Maximum Error Caused by Direction Choice

Mario Barbatti

► **To cite this version:**

Mario Barbatti. Velocity Adjustment in Surface Hopping: Ethylene as a Case Study of the Maximum Error Caused by Direction Choice. *Journal of Chemical Theory and Computation*, 2021, 10.1021/acs.jctc.1c00012 . hal-03204599

HAL Id: hal-03204599

<https://hal.science/hal-03204599>

Submitted on 21 Apr 2021

HAL is a multi-disciplinary open access archive for the deposit and dissemination of scientific research documents, whether they are published or not. The documents may come from teaching and research institutions in France or abroad, or from public or private research centers.

L'archive ouverte pluridisciplinaire **HAL**, est destinée au dépôt et à la diffusion de documents scientifiques de niveau recherche, publiés ou non, émanant des établissements d'enseignement et de recherche français ou étrangers, des laboratoires publics ou privés.



Distributed under a Creative Commons Attribution - NonCommercial - NoDerivatives 4.0 International License

Velocity Adjustment in Surface Hopping: Ethylene as a Case Study of the Maximum Error Caused by Direction Choice

Mario Barbatti*

Cite This: <https://doi.org/10.1021/acs.jctc.1c00012>

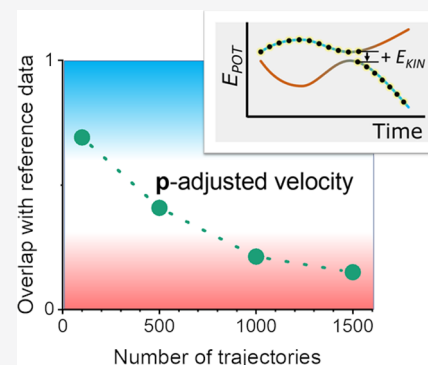
Read Online

ACCESS |

Metrics & More

Article Recommendations

ABSTRACT: The most common surface hopping dynamics algorithms require velocity adjustment after hopping to ensure total-energy conservation. Based on the semiclassical analysis, this adjustment must be made parallel to the nonadiabatic coupling vector's direction. Nevertheless, this direction is not always known, and the common practice has been to adjust the velocity in either the linear momentum or velocity directions. This paper benchmarks surface hopping dynamics of photoexcited ethylene with velocity adjustment in several directions, including those of the nonadiabatic coupling vector, the momentum, and the energy gradient difference. It is shown that differences in time constants and structural evolution fall within the statistical uncertainty of the method considering up to 500 trajectories in each dynamics set, rendering the three approaches statistically equivalent. For larger ensembles beyond 1000 trajectories, significant differences between the results arise, limiting the validity of adjustment in alternative directions. Other possible adjustment directions (velocity, single-state gradients, angular momentum) are evaluated as well. Given the small size of ethylene, the results reported in this paper should be considered an upper limit for the error caused by the choice of the velocity-adjustment direction on surface hopping dynamics.



I. INTRODUCTION

Surface hopping dynamics is often used for computational investigations of nonadiabatic processes in photoexcited molecules.^{1,2} In this method, hopping probabilities between electronic states are evaluated, and a stochastic algorithm decides on which surface the dynamics should be propagated at each time step. An ensemble of surface hopping trajectories is expected to reproduce the quantum nuclear wavepacket split between different states due to nonadiabatic couplings.³

At the hopping time, the energy difference between the potential energy surfaces is typically a fraction of electron volt. To ensure energy conservation in independent-trajectory surface hopping algorithms—like the popular fewest-switches surface hopping⁴—an equivalent amount of nuclear kinetic energy is added (when hopping to a lower state) or removed (when hopping to a higher state). The usual prescription in surface hopping has been well established by short-time analysis of nonadiabatic semiclassical propagation.^{5,6} It consists of balancing energy by adjusting the nuclear velocity in the direction of the nonadiabatic coupling vector between the current (L) and target (J) electronic states⁴

$$\mathbf{h}_{JL} = \langle J | \nabla_{\mathbf{R}} L \rangle \quad (1)$$

Thus, the potential energy variation at the hopping event translates into the work of a force acting on the nuclei in this particular direction. This formulation stems from the semiclassical Pechukas force⁷

$$\mathbf{F}_{LJ}^P = -\text{Re} \left[\frac{\langle \psi^J(t, t'') | \nabla_{\mathbf{R}(t)} H_{el}(t) | \psi^L(t, t') \rangle}{\langle \psi^J(t, t'') | \psi^L(t, t') \rangle} \right] \quad (2)$$

driving the molecular system from electronic state L to state J along a stationary nuclear phase $\bar{\mathbf{R}}(t)$ starting at t' and ending at t'' . In the mixed quantum-classical formulation of Coker and Xiao,⁸ the Pechukas force acting during one time step Δt simplifies to

$$\mathbf{F}_{LJ}^P(t') \approx - \left[\frac{1}{\Delta t} \frac{(E_J - E_L)}{\hat{\mathbf{h}}_{JL} \cdot \mathbf{v}} \right] \hat{\mathbf{h}}_{JL} \quad (3)$$

where $\hat{\mathbf{h}}_{JL} = \mathbf{h}_{JL}/h_{JL}$ is the unitary direction along the nonadiabatic coupling vector, \mathbf{v} is the nuclear velocity, and E_J and E_L are the potential electronic energies. In this case, the work done by the Pechukas force during the nonadiabatic transitions is approximately

$$\mathbf{F}_{LJ}^P(t') \cdot \mathbf{v} \Delta t = E_L - E_J \quad (4)$$

Received: January 6, 2021

corresponding exactly to the potential energy gap between the adiabatic states.

Nevertheless, there are implementations of surface hopping where the nonadiabatic coupling vector direction is unknown. For instance, this happens when the nonadiabatic coupling is evaluated using the time-derivative coupling $\sigma_{JL} = \langle J | \frac{\partial}{\partial t} L \rangle$,⁹ which is a scalar quantity. This time-derivative coupling became a popular option in surface hopping because, while nonadiabatic coupling vectors are unavailable for many electronic structure methods, it can be computed from approximated wave function overlaps.^{10–13} The nonadiabatic coupling direction is also usually unknown when using local diabaticization,^{14,15} in which the nonadiabatic propagation is, as before, based on wave function overlaps. Other surface hopping variants estimate nonadiabatic transition probabilities based only on the topography of the potential energy surfaces, as in the Zhu–Nakamura^{16,17} and Belyaev–Lebedev (adiabatic Landau–Zener) approaches.^{18–20}

If the nonadiabatic coupling vector is unknown, it is usual to balance energy by rescaling the nuclear velocity either in the momentum or velocity direction. In Zhu–Nakamura surface hopping,¹⁶ the adjustment is made perpendicular to the crossing seam's direction, which is estimated from the gradients of the potential energy gap. Although such prescriptions do not match the Pechukas condition, they all have been thought not to introduce much of an error due to the small energy gaps at the hopping time.

Nevertheless, there is cumulative evidence that the vibrational energy redistribution in the direction of the nonadiabatic coupling vector may play a bigger role than usually expected. Fernandez-Alberti, Tretiak, and co-workers have shown for several classes of systems that the vibrational energy relaxation after a nonadiabatic transition is biased toward the nonadiabatic coupling vector's direction.^{21–23} Their analysis of vibrational energy redistribution revealed that only a small subset of normal modes with large overlap with the nonadiabatic coupling vector actively contributes to the electronic relaxation process. Sellner and co-workers²⁴ have also shown that the exit direction from the conical intersection may be the main driver for forming specific photoproducts. All of these results imply that an accurate description of the energy redistribution after hopping is crucial for reliable nonadiabatic dynamics simulations.

The question that arises is how much impact on the dynamics the velocity-adjustment direction has. A study by Plasser et al.²⁵ based on surface hopping on analytical potential energy surfaces indicated that adjusting the velocity either in the nonadiabatic coupling vector or velocity directions led to different quantitative outputs for the SO₂ dynamics, although within the statistical margin of error of their 200 trajectories. Moreover, Ibele and Curchod²⁶ have recently reported some significant differences between surface hopping results for fulvene after adjusting the velocity either in the nonadiabatic coupling vector or velocity direction. Nevertheless, their trajectory ensemble composed of 18 initial conditions repeated 10 times each does not provide a definitive basis to draw reasonable statistical conclusions.

In any case, this body of evidence pointing to a potential impact of the velocity-adjustment direction on the dynamics is worrisome. How reliable are all of those dynamics based on methods like TD-DFT and ADC(2), invariably balancing energy in directions other than that of the nonadiabatic coupling vector?

I could not find a clear answer in the published studies. For this reason, I decided to compute a benchmark of results especially tailored to evaluate the impact of the velocity-adjustment direction on surface hopping. This benchmark is the subject of this paper, which I believe will help the many research groups running nonadiabatic dynamics simulations.

Note that it is not my goal to discuss which direction is the most adequate to make the velocity adjustment. This point is clearly settled; it is the nonadiabatic coupling vector's direction. I want to address the following question: considering that actual simulations based on on-the-fly electronic-structure calculations are done with relatively small trajectory ensembles, are the errors due to the velocity-adjustment direction statistically significant?

For the benchmark, I worked on ethylene, C₂H₄. Its small size, ultrafast dynamics (<100 fs) through a conical intersection, and massive conformational flexibility have made this molecule a favorite system for benchmarks and testing method developments, including wavepacket dynamics on multidimensional analytical surfaces,²⁷ on-the-fly quasi-diabatic dynamics,²⁸ multiple spawning on CASSCF,²⁹ CASPT2,^{30,31} and approximated DFT³² surfaces, multiconfigurational Ehrenfest,³³ surface hopping on semiempirical,^{34,35} ΔSCF–Kohn–Sham,^{36,37} floating-occupation CASCI,³⁸ CASSCF,²⁶ and MRCI³⁹ surfaces, and surface hopping with electron–nucleus correlation.⁴⁰ The small size of ethylene should also amplify any effects of the velocity-adjustment direction, helping to detect them. Finally, the excited-state surface topography near the crossing seam of ethylene is a prototype for the conical intersections in many other organic systems, even aromatic rings, where “ethylenic intersections” are a recurrent pattern.⁴¹

II. COMPUTATIONAL DETAILS

II.I. Electronic Structure and Dynamics. All calculations were done with the multiconfigurational self-consistent field (MCSCF). The total active space was composed of five separate complete active subspaces: the first subspace contained four electrons and four orbitals (π , σ , π^* , σ^*), and each of the four other subspaces contained two electrons in two orbitals (σ , σ^*). The rationale for using this $[\text{CAS}(4,4) \oplus 4 \times \text{CAS}(2,2)]$ space is that it allows describing the lowest singlet excited valence states ($\pi\pi^*$ and $\pi\sigma^*$) in the CAS(4,4) subspace, giving enough conformational flexibility through the (σ, σ^*) pairs in the CAS(2,2) subspaces. Because excitations are restricted to within the subspace, the total number of configuration state functions (CSFs) is only 3012, much smaller than the 226512 CSFs of a complete active space containing the same 12 electrons and 12 orbitals. Three states were computed with a state average procedure (SA-3). The 6-31G* basis set was used.⁴² These calculations do not account for dynamic electron correlation, which is not a problem for this benchmark's goals.

Dynamics was simulated with decoherence-corrected⁴³ fewest-switches surface hopping⁴ (DC-FSSH). The classical equations of motion were integrated with a 0.1 fs time step for a maximum of 200 fs. The quantum equations were integrated with 0.005 fs steps, using interpolated electronic quantities between classical steps. Decoherence corrections were applied with the simplified decay of mixing approach,⁴³ with the standard 0.1 a.u. parameter. Frustrated hoppings and velocity adjustment are reviewed and discussed in more detail in subsection II.III.

Three sets of 500 trajectories each were run. The initial conditions for dynamics were sampled from a harmonic oscillator Wigner distribution of the nuclei. The corresponding

absorption spectrum is shown in Figure 1. The bright $\pi\pi^*$ state was the S_1 adiabatic state in all geometries sampled in this way.

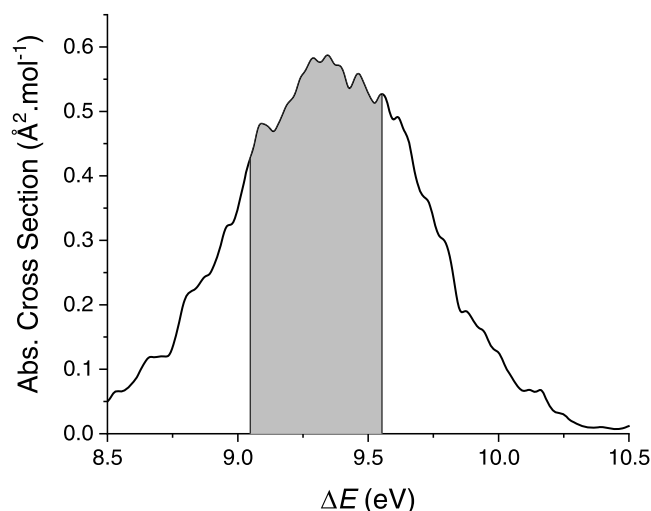


Figure 1. Computed absorption spectrum of ethylene based on a 2400-point nuclear ensemble. Initial conditions for dynamics were sampled from the shaded area.

Trajectories were started in S_1 exclusively from a subset of geometries constrained to the 9.30 ± 0.25 eV excitation-energy window. Selection within this excitation-energy window yielded 1079 initial conditions, from which 500 were used to initiate the trajectories. All trajectories used the same sequence of pseudo-random numbers to feed the DC-FSSH algorithm.

The MCSCF calculations were done with Columbus (version 7, 09-Oct-2020).^{44,45} Dynamics was done with Newton-X (version 2.2 build 12)^{46,47} interfaced to Columbus. All Newton-X input and output files for the three sets of dynamics are available for download.⁴⁸

II.II. Data Analysis. For each set, the mean population of electronic state I at time t was computed as

$$\rho_I(t) = \frac{1}{N_{surv}(t)} \sum_{n=1}^{N_{surv}} |c_I^{(n)}(t)|^2 \quad (5)$$

where $c_I^{(n)}(t)$ is the complex time-dependent coefficient of the electronic wave function for the state I of trajectory n . As trajectories may end before the maximum time due to error in the MCSCF calculation, the mean population at time t is computed averaging over the $N_{surv}(t)$ surviving trajectories at that time.

Another quantity of interest is the mean oscillator strength of the current state, which is computed as

$$\bar{f}_{curr}(t) = \frac{1}{N_{traj}} \sum_{n=1}^{N_{traj}} f_{L0}^{(n)}(t) \quad (6)$$

where $f_{L0}^{(n)}(t)$ is the oscillator strength between the ground state (0) and the current excited state of trajectory n at time t ($L = 1$ or 2). If the current state is the ground state, $f_{L0}^{(n)}(t)$ is taken as zero (which means that ground-state excitation is neglected). For times after the trajectory's ending time, $f_{L0}^{(n)}(t)$ is also assumed to be zero. The average is computed over all N_{traj} trajectories in the set.

The mean S_1 populations and mean current state's oscillator strengths were fitted with the function

$$f(t) = N_0 + (N_1 - N_0) \exp\left(-\frac{t - t_L}{t_E}\right) \quad (7)$$

The lifetime is

$$\tau = t_L + t_E \quad (8)$$

and the margins of error for the sample average were computed as

$$\delta\tau = \frac{Z}{\sqrt{N_{traj}}} \tau \quad (9)$$

where Z is 1.96 for the 95% confidence interval and τ (the exponential time constant) is also the standard deviation of the distribution. Fitting the populations, N_1 was fixed at 1. Fitting oscillator strengths, t_L and N_0 were fixed at 0.

Structural analysis was done at the last step of each trajectory and after 20 fs of (not necessarily consecutive) S_0 dynamics. The number η_1 of hydrogen atoms bound to carbon C1 was computed by counting the number of H atoms closer than 2 Å to C1 and also closer to C1 than to C2. An equivalent definition was applied to η_2 , the number of H atoms bound to C2. Structures were classified as indicated in Table 1.

Table 1. Structure Definition According to the Number of Hydrogen Atoms Bound to C1 (η_1) and C2 (η_2)

η_1	η_2	structure
2	2	ethylene
3	1	ethylidene
1	3	
3	0	H dissociation
0	3	
2	1	
1	2	
2	0	2H dissociation
0	2	
1	1	

The proportion p_i of each type of structure listed in Table 1 in the trajectory ensemble was computed, and the margin of errors for the sample proportion is

$$\varepsilon = Z \sqrt{\frac{p_i(1 - p_i)}{N_{traj}}} \quad (10)$$

As before, Z is 1.96 for the 95% confidence interval.

II.III. Conservation of Total Energy. In this section, I review the standard way velocity is adjusted after hopping to conserve the total energy. If a hopping event occurs from a state L to a state J , through a potential energy gap $\Delta E_{LJ} = E_J - E_L$, conservation of the total energy can be ensured by applying the constraint that the variation of kinetic energy, $\Delta K_{LJ} = K_J - K_L$, is equal to the variation of potential energy

$$\Delta K_{LJ} = -\Delta E_{LJ} \quad (11)$$

In practice, this constraint is imposed by changing the velocity of the nucleus α as⁴⁹

$$\mathbf{v}_\alpha^{(J)} = \mathbf{v}_\alpha^{(L)} + \gamma_{LJ} \frac{\mathbf{u}_\alpha}{M_\alpha} \quad (12)$$

where \mathbf{u}_α is a vector indicating the direction along which the change should be applied and M_α is the nuclear mass. With the aid of eq 12, the kinetic energy variation should be

$$\Delta K_{LJ} \equiv \frac{1}{2} \sum_{\alpha} M_{\alpha} (\mathbf{v}_{\alpha}^{(J)})^2 - \frac{1}{2} \sum_{\alpha} M_{\alpha} (\mathbf{v}_{\alpha}^{(L)})^2 = \gamma_{LJ}^2 a + \gamma_{LJ} b \quad (13)$$

where

$$a \equiv \frac{1}{2} \sum_{\alpha} \frac{\mathbf{u}_{\alpha} \cdot \mathbf{u}_{\alpha}}{M_{\alpha}}$$

$$b \equiv \sum_{\alpha} (\mathbf{v}_{\alpha}^{(L)} \cdot \mathbf{u}_{\alpha}) \quad (14)$$

If we replace eq 13 in 11, we obtain

$$a\gamma_{LJ}^2 + b\gamma_{LJ} + \Delta E_{LJ} = 0 \quad (15)$$

which can be solved for γ_{LJ} . If $\Delta \equiv b^2 - 4a\Delta E_{LJ} < 0$, there are no real solutions, and the hopping is frustrated. In the present simulations, the momentum direction was not changed after such a frustrated hopping. On the other hand, if $\Delta \geq 0$,

$$\gamma_{LJ} = \begin{cases} \frac{-b + \sqrt{\Delta}}{2a} & \text{if } |-b + \sqrt{\Delta}| < |-b - \sqrt{\Delta}| \\ \frac{-b - \sqrt{\Delta}}{2a} & \text{if } |-b + \sqrt{\Delta}| \geq |-b - \sqrt{\Delta}| \end{cases} \quad (16)$$

Equation 16 is set to choose the minimum value of γ_{LJ} , thus reducing the velocity-adjustment interference in the dynamics. Alternatively, Polli, Weingart, and co-workers^{50,51} proposed to choose the global sign of \mathbf{u}_{α} in such a way that this vector has a positive overlap with $\mathbf{v}_{\alpha}^{(L)}$. With this choice, minimum interference is achieved by selecting the second eq 16. In the present work, I followed the former formulation, which is implemented in Newton-X.

For the benchmark, I have run three sets of trajectories, each one with the direction \mathbf{u} defined as follows:

1. **h-adjusted set:** Velocity adjustment in the direction of the nonadiabatic coupling vector \mathbf{h}_{JL} . This should be the standard prescription for surface hopping whenever \mathbf{h}_{JL} is available. In this case, $\mathbf{u}_{\alpha} = \mathbf{h}_{JL,\omega}$ where $\mathbf{h}_{JL,\alpha} = \langle J | \nabla_{\alpha} L \rangle \cdot |L\rangle$ and $|J\rangle$ are the electronic wave functions of the current (L) and target (J) states.
2. **p-adjusted set:** Velocity adjustment in the direction of the linear momentum \mathbf{p} . This prescription is often used when \mathbf{h}_{JL} is unknown. In this case, $\mathbf{u}_{\alpha} = \mathbf{p}_{\omega}$ where $\mathbf{p}_{\alpha} = M_{\alpha} \mathbf{v}_{\alpha}$.
3. **g-adjusted set:** Velocity adjustment in the direction of the gradient difference vector \mathbf{g}_{JL} . The branching space around a conical intersection is defined by \mathbf{h}_{JL} and \mathbf{g}_{JL} .³ When \mathbf{h}_{JL} is unknown, \mathbf{g}_{JL} may be a good alternative for velocity adjustment. In this case, $\mathbf{u}_{\alpha} = \mathbf{g}_{JL,\omega}$ where $\mathbf{g}_{JL,\alpha} = \nabla_{\alpha} E_J - \nabla_{\alpha} E_L$.

III. RESULTS AND DISCUSSION

III.I. Ethylene Dynamics. MCSCF-based surface hopping dynamics of ethylene has been discussed in detail before.³⁹ The results obtained here are equivalent to those in that previous work, and I will just summarize the key points relevant to our discussion of the velocity adjustment. In this subsection, I will focus on the **h**-adjusted results, while in the next subsection, I will compare them to the **p**- and **g**-adjusted ones.

Upon excitation into the ${}^1\pi\pi^*$ (S_1) state, the DC-FSSH/MCSCF simulations predict that the depopulation of the S_1 adiabatic state toward S_0 follows an exponential decay pattern, which starts 15 fs after the excitation, with an exponential time constant of 99 fs. These values are obtained by fitting the mean S_1 population with eq 7. The fitting parameters are summarized in Table 2. During the excited-state dynamics, the S_2 state gets

Table 2. Fitting Parameters (eq 7) of the Mean S_1 Population and Current State's Mean Oscillator Strength for the Three Sets of Trajectories

	N_I	N_0	t_L (fs)	t_E (fs)	τ (fs)
	Population				
h set	1	0	15	99	114 ± 10
p set	1	0	14	106	120 ± 11
g set	1	0	14	116	130 ± 11
	Osc. Strength				
h set	0.44	0	0	15	15 ± 2
p set	0.42	0	0	17	17 ± 2
g set	0.42	0	0	17	17 ± 2
expt. ^{52–57}					10 – 30

about 20% of the population within the first 25 fs (Figure 2), but it is quickly deactivated too. The S_0 state is populated within 114 fs.

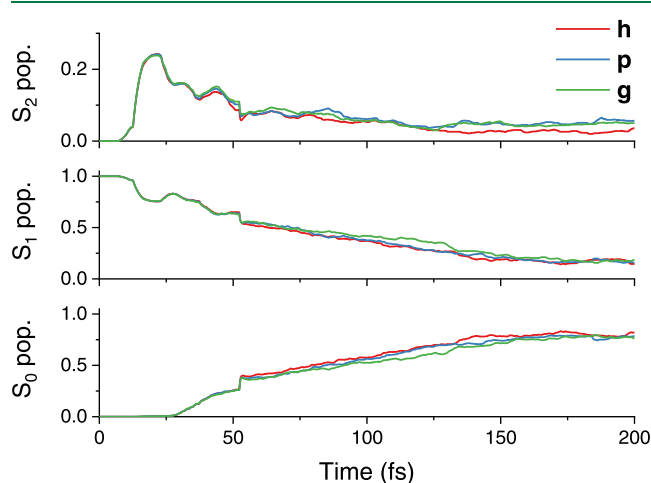


Figure 2. Mean populations of the S_0 (bottom), S_1 (middle), and S_2 (top) adiabatic states as a function of time for the three sets of trajectories.

Time-resolved spectroscopy has shown that ethylene's internal conversion occurs in only 10–30 fs,^{52–56} making it one of the fastest internal conversion processes known. This time constant is much shorter than the 114 fs predicted by the simulations. The reason for this discrepancy is that the experimental time constant reflects diabatic features of the excited states, as the probe process (usually) depends on excited-state ionization or stimulated emission probabilities, depending on the setup.³¹ Therefore, to estimate the diabatic-state decay time constant, we can monitor the time evolution of the current state's oscillator-strength mean value (eq 6). This quantity is plotted in Figure 3, and it decays exponentially with a 15 fs time constant (Table 2), in excellent agreement with the experiments.

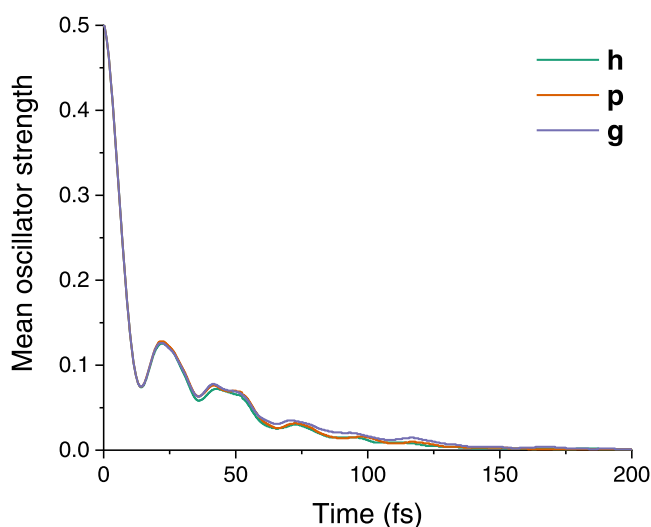


Figure 3. Current state's mean oscillator strength as a function of time for the three trajectory sets.

The current state's mean oscillator-strength evolution in [Figure 3](#) shows some damped oscillations with a period of approximately 20 fs. Fast Fourier transform of this signal revealed three frequencies, 500, 830, and 1300 cm^{-1} ($\pm 160 \text{ cm}^{-1}$). These oscillations correspond to coherent classical vibrational motions, which have also been observed in previous wavepacket²⁷ and surface hopping^{34,35} simulations. They have been experimentally detected by Kosma and co-workers,⁵⁶ who reported frequencies of 631, 1113, and 1572 cm^{-1} , and Kobayashi et al.,⁵⁷ who measured a revival in the photoelectron intensity with an 18-fs period.

The energy gaps at the hopping time show a broad distribution of values ([Table 3](#)). The $S_1 \rightarrow S_0$ hoppings, for example, are nearly exponentially distributed with a 0.65 eV mean energy gap ([Figure 4](#)). The $S_2 \rightarrow S_1$ hopping distribution deviates from an exponential and peaks at 0.3 eV with a 0.39 eV mean value. Hoppings may occur over some very large energy gaps too. The mean value of the few $S_2 \rightarrow S_0$ hoppings is 4.93 eV, for instance. Such large gaps always correspond to the sample of tiny random numbers in the stochastic hopping algorithm. For instance, the 500 trajectories in the **h**-adjusted data set had eight hoppings with anomalously large absolute energy gaps between 5 and 6 eV. They all occurred with probabilities smaller than 2×10^{-6} .

It may look surprising that the $S_1 \rightarrow S_2$ and $S_1 \rightarrow S_0$ hopping counts in [Table 3](#) differ between the three sets. This difference arises from the fact that this count includes the first hopping and occasional latter hoppings between the same states. For instance,

43% of trajectories in the **h**-adjusted data set undergo more than one $S_1 \rightarrow S_2$ hopping.

Compared to the total kinetic energy K_L before hopping, the distribution of energy gaps ΔE_{IJ} in [Table 3](#) indicates that for a molecule as small as ethylene, the velocity adjustment leads to a considerable kinetic-energy change. For $S_1 \rightarrow S_0$, $S_0 \rightarrow S_1$, and $S_2 \rightarrow S_1$, $|\Delta E_{IJ}|/K_L$ is distributed exponentially, with mean values of 0.30, 0.22, and 0.24, respectively (considering all trajectories in the **h**-adjusted data set). For $S_1 \rightarrow S_2$, the distribution peaks at 0.25 with a mean value of 0.29.

After returning to the ground state, ethylene transfers all photon energy to the vibrational modes, and it tends to dissociate. At the last step of the full trajectory ensemble, a third of the population releases one H (31%) or two H (3%) atoms ([Table 4](#)). Ethylidene isomer (CH_3CH) is also a common photoproduct (18%). Within the simulation time, ethylene is still the most common structure, with 38% in the ground state and 9% in the excited states.

[Table 4](#) also reports the structural analysis after the system remains for 20 fs in the ground state. Due to the large amount of energy deposited in the ground-state vibrational modes, ethylene also quickly reaches distorted geometries. When this happens, the MCSCF calculation may either not converge or radically change the active space, causing a total energy discontinuity. Thus, many trajectories die before the maximum termination time of 200 fs. For the **h**-adjusted set, 349 trajectories run in the ground state for 20 fs or longer. Considering that 47 trajectories ended still in the excited state, 104 trajectories finished in S_0 but without completing 20 fs there. The structural distribution at 20 fs is qualitatively the same as at the end of the trajectory. (Note that the 20-fs data do not consider excited fragments in the fraction estimate.) Most of the ground-state structures (43%) are CH_2CH_2 . The amount of ethylidene is 20%. Single and double H dissociations contribute 32 and 5% of the total, respectively.

III.II. Velocity-Adjustment Effect. The results of surface hopping dynamics of ethylene adjusting the velocity in the **p** and **g** directions yield the same picture as described in the previous subsection, with the quantitative agreement within the margin of errors computed for the 95% confidence interval, as we can verify in [Table 2](#) for time constants, [Table 3](#) for hopping distributions, and [Table 4](#) for structural evolution.

Nevertheless, it seems that adjustment along **p** yields better agreement with the reference **h**-adjusted set than making it along **g**. Note, for example, the adiabatic time constants in [Table 2](#): the **p**-adjusted value (120 ± 11 fs) compares much better to the **h**-adjusted value (114 ± 10 fs) than the **g**-adjusted value (130 ± 11 fs).

To check quantitatively how good the agreement is between two sets of trajectories, we can estimate the probability that they

Table 3. Number of Hoppings and Hopping Energy-Gap Absolute Mean Value and Standard Deviation for the Three Sets of Trajectories

	h set			p set			g set		
	count	mean (eV)	st. dev. (eV)	count	mean (eV)	st. dev. (eV)	count	mean (eV)	st. dev. (eV)
$S_2 \rightarrow S_1$	259	0.39	0.28	252	0.43	0.32	255	0.41	0.32
$S_2 \rightarrow S_0$	18	4.93	0.47	20	4.91	0.97	19	4.86	0.64
$S_1 \rightarrow S_2$	281	0.63	0.43	285	0.62	0.42	277	0.62	0.44
$S_1 \rightarrow S_0$	618	0.65	0.88	613	0.61	0.85	622	0.63	0.85
$S_0 \rightarrow S_2$	2	2.12	0.29	6	1.88	0.19	5	1.88	0.14
$S_0 \rightarrow S_1$	181	0.76	0.86	187	0.70	0.82	205	0.72	1.01

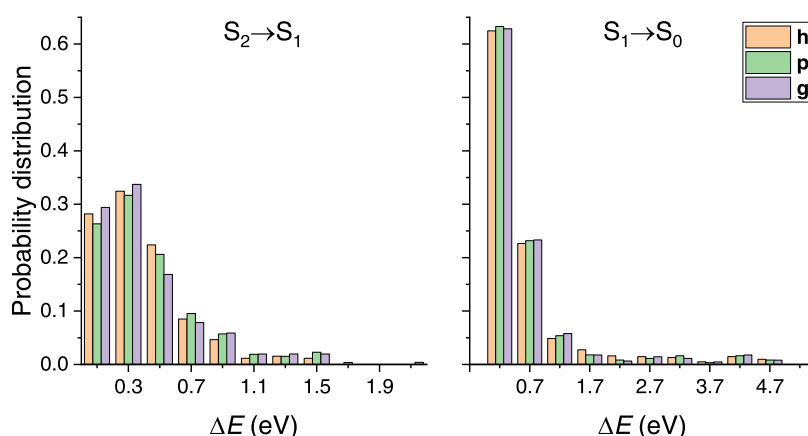


Figure 4. Probability distribution of potential energy gaps at the hopping times for the $S_2 \rightarrow S_1$ (left) and $S_1 \rightarrow S_0$ (right) transitions, for the three sets of trajectories.

Table 4. Structural Analysis (%) of the Trajectories at the Last Time Step and after Staying for 20 fs in S_0^a

fragments (%)	state	h set	p set	g set
At the Last Step				
CH ₂ CH ₂	S_2, S_1	9 ± 3	12 ± 3	14 ± 3
CH ₂ CH ₂	S_0	38 ± 4	41 ± 4	42 ± 4
CH ₃ CH	S_0	18 ± 3	15 ± 3	15 ± 3
C ₂ H ₃ + H	S_0	31 ± 4	27 ± 4	26 ± 4
C ₂ H ₂ + 2H	S_0	3 ± 1	3 ± 1	3 ± 1
N_{traj}		500	500	500
After 20 fs in S_0				
CH ₂ CH ₂	S_0	43 ± 5	47 ± 5	46 ± 5
CH ₃ CH	S_0	20 ± 3	21 ± 4	21 ± 4
C ₂ H ₃ + H	S_0	32 ± 5	29 ± 5	29 ± 5
C ₂ H ₂ + 2H	S_0	5 ± 2	4 ± 2	35 ± 2
N_{traj}		349	326	316

^aDissociation was considered with a 2 Å criterium.

will both yield overlapping results within the confidence interval (Figure 5a). To do so, we proceed in the following way. First, we determine the overlap interval $[\omega_{start}, \omega_{end}]$ between the same observable x predicted by ensembles (1) and (2), comparing its mean values μ and error bars ϵ

$$\begin{aligned} \omega_{start} &= \max[\mu^{(1)} - \epsilon^{(1)}, \mu^{(2)} - \epsilon^{(2)}] \\ \omega_{end} &= \min[\mu^{(1)} + \epsilon^{(1)}, \mu^{(2)} + \epsilon^{(2)}] \end{aligned} \quad (17)$$

If $\omega_{end} \leq \omega_{start}$ the overlap is null.

The probability that the observable predictions in the two sets fall in the overlap between the confidence interval is

$$\begin{aligned} P_x^{(1,2)} &= P_x^{(1)} \times P_x^{(2)} \\ &= \left[\frac{Z}{\epsilon^{(1)} \sqrt{2\pi}} \int_{\omega_{start}}^{\omega_{end}} e^{-Z^2[(x-\mu^{(1)})/\epsilon^{(1)}]^2/2} dx \right] \\ &\quad \times \left[\frac{Z}{\epsilon^{(2)} \sqrt{2\pi}} \int_{\omega_{start}}^{\omega_{end}} e^{-Z^2[(x-\mu^{(2)})/\epsilon^{(2)}]^2/2} dx \right] \end{aligned} \quad (18)$$

Solving these integrals results in

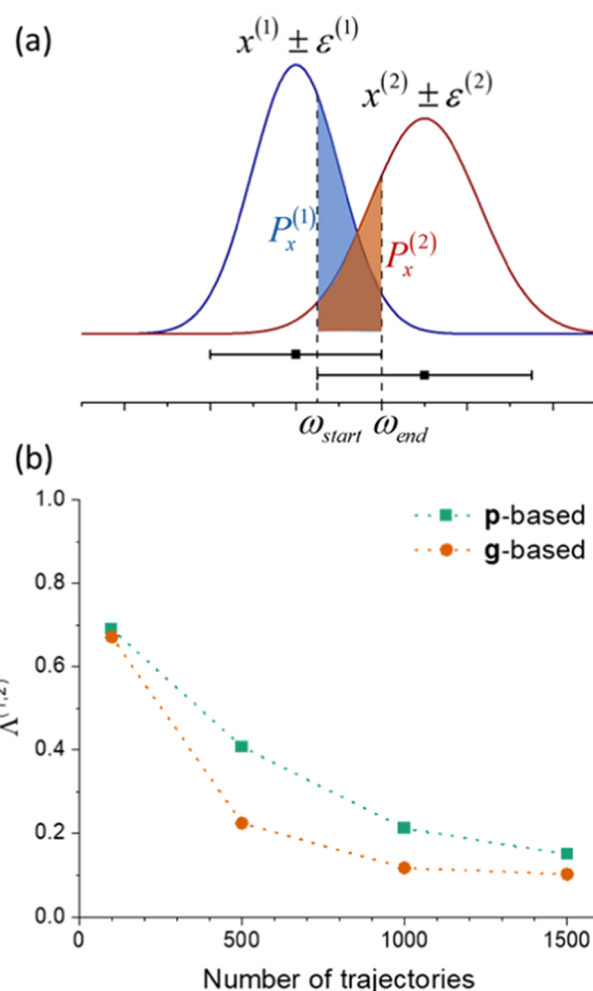


Figure 5. (a) Illustration of an observable $x \pm \epsilon$ predicted by two trajectory sets (1) and (2). The shaded areas correspond to the probabilities of this observable of falling within the overlap region determined by the confidence interval. (b) Mean overlap score $\Lambda^{(1,2)}$ over an ensemble of seven observables as a function of the number of trajectories, comparing p- and g-adjusted sets to the h-adjusted set. $\Lambda^{(1,2)}$ near unity means that the two sets yield statistically equivalent results within a 95% confidence interval. $\Lambda^{(1,2)}$ near zero means that results from the two sets do not match within the same interval.

$$\begin{aligned}
 P_x^{(1,2)} = & \frac{1}{2} \left[\operatorname{erf} \left(\frac{\sqrt{2} Z(-\omega_{\text{start}} + \mu^{(1)})}{2\epsilon^{(1)}} \right) \right. \\
 & \left. - \operatorname{erf} \left(\frac{\sqrt{2} Z(-\omega_{\text{end}} + \mu^{(1)})}{2\epsilon^{(1)}} \right) \right] \\
 & \times \frac{1}{2} \left[\operatorname{erf} \left(\frac{\sqrt{2} Z(-\omega_{\text{start}} + \mu^{(2)})}{2\epsilon^{(2)}} \right) \right. \\
 & \left. - \operatorname{erf} \left(\frac{\sqrt{2} Z(-\omega_{\text{end}} + \mu^{(2)})}{2\epsilon^{(2)}} \right) \right] \quad (19)
 \end{aligned}$$

Naturally, $P_x^{(1,2)} = 0$ if $\omega_{\text{end}} \leq \omega_{\text{start}}$. The maximum probability occurs when both sets predict the same mean value and error bars. In this case, $P_{\text{max}}^{(1,2)} = 0.95 \times 0.95 = 0.9025$. Thus, we can introduce an overlap score for variable x , defined as $\lambda_x \equiv P_x^{(1,2)} / P_{\text{max}}^{(1,2)}$. The mean overlap score over an ensemble of N_o observables is

$$\Lambda^{(1,2)} = \frac{1}{N_o} \sum_x \lambda_x^{(1,2)} \quad (20)$$

$\Lambda^{(1,2)}$ is near one if the predictions of both sets significantly overlap and zero if they do not.

$\Lambda^{(1,2)}$ was computed considering seven observables: the adiabatic-population and oscillator-strength time constants in Table 2 and the five structural channels calculated at the trajectories' last step given in Table 4. The results are 0.41 for the **p**–**h** comparison and 0.23 for the **g**–**h** comparison (Figure 5b, 500 trajectories), confirming that the **p**-adjustment is superior to the **g**-adjustment.

The dependence of $\Lambda^{(1,2)}$ on the number of trajectories in each set can be estimated by supposing that the mean value remains constant and the margin of error changes according to $\epsilon_{N_{\text{traj}}} = \sqrt{500/N_{\text{traj}}} \epsilon_{500}$, where ϵ_{500} is the margin of error for 500 trajectories. $\Lambda^{(1,2)}$ for a new N_{traj} can be recomputed by replacing this margin of error in eqs 17 and 18.

$\Lambda^{(1,2)}$ as a function of the number of trajectories is shown in Figure 5b. For a small ensemble of 100 trajectories, both **p**- and **g**-adjusted sets have excellent overlaps with the reference **h**-adjusted set. Due to the large margin of errors, it does not matter how the adjustment is made. For 500 trajectories, the agreement with the **h** set worsens for both **p**- and **g**-sets, but the **p**-adjusted results are more reliable. For 1500 trajectories, **p**- and **g**-adjusted results are both not very reliable.

To understand why the **p**-adjusted set generally does better than the **g**-adjusted set when compared to the **h**-adjusted set, we look at the projection of the **p** and \mathbf{g}_{JL} on \mathbf{h}_{JL} at the hopping time. A large projection should reduce the error compared to a small projection, as the adjustment is made in a direction closer to that of \mathbf{h}_{JL} . Thus, for each $S_L \rightarrow S_j$ hopping in the **h** set, the absolute value of the projection of a vector **q** on \mathbf{h}_{JL} was computed as

$$P_{qh} = \left| \frac{\mathbf{q} \cdot \mathbf{h}_{JL}}{q h_{JL}} \right| \quad (21)$$

where **q** is either **p** or \mathbf{g}_{JL} .

The area-normalized histograms for both projections (corresponding to the probability distribution) at the $S_1 \rightarrow S_0$ hoppings are shown in Figure 6. P_{gh} peaks at 0 with a 0.29 mean projection, while P_{ph} has a flat peak between 0.2 and 0.7 with a

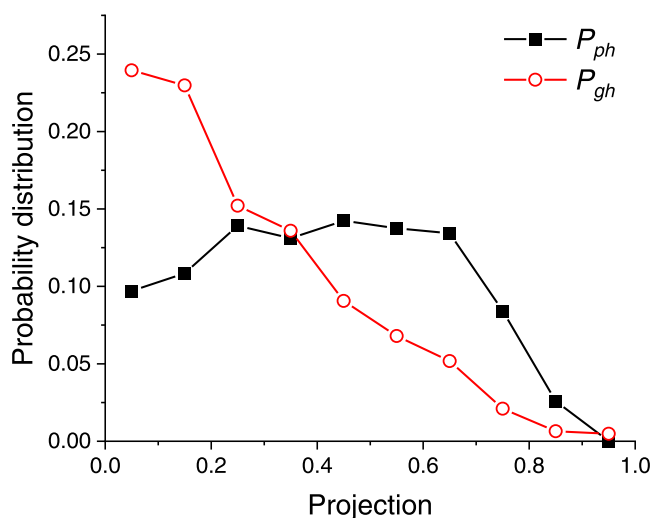


Figure 6. Probability distribution of **p** and \mathbf{g}_{01} projections on \mathbf{h}_{01} at the $S_1 \rightarrow S_0$ hopping time for the **h**-adjusted set.

0.41 mean. These distributions are qualitatively expected. The hopping probability is proportional to $\mathbf{v} \cdot \mathbf{h}_{01}$,⁴ which means that, at the hopping time, the momentum should have a large projection on \mathbf{h}_{01} . On the other hand, near the crossing seam, \mathbf{g}_{01} tends to be orthogonal to \mathbf{h}_{01} ,⁵⁸ yielding a distribution peaking at zero.

The distributions in Figure 6 imply that the probability is larger of having bigger projections of **p** on \mathbf{h}_{01} than of \mathbf{g}_{01} on \mathbf{h}_{01} . However, momentum is better than the gradient difference vector for hopping between S_0 and S_1 only. Vector \mathbf{g}_{JL} in turn, has bigger mean projections on \mathbf{h}_{JL} for hoppings between S_1 and S_2 (Table 5). Nevertheless, because $S_1 \rightarrow S_0$ hoppings are by far

Table 5. Mean Values (and Standard Deviations) of the P_{qh} Projections of Linear Momentum (**p**), Nuclear Velocity (**v**), Energy Gradient Difference (\mathbf{g}_{JL}), Energy Gradient of the Current State S_L (\mathbf{g}_L), Energy Gradient of the Target State S_j (\mathbf{g}_j), and Angular Momentum (**L**) on the Nonadiabatic Coupling Vector \mathbf{h}_{JL} at the $S_L \rightarrow S_j$ Hopping Time for the **h**-Adjusted Set

vector	$S_1 \rightarrow S_0$	$S_2 \rightarrow S_1$	$S_0 \rightarrow S_1$	$S_1 \rightarrow S_2$	all hops
\mathbf{h}_{JL}	1	1	1	1	1
p	0.41 (0.22)	0.34 (0.20)	0.42 (0.23)	0.41 (0.25)	0.40 (0.23)
v	0.32 (0.17)	0.41 (0.26)	0.23 (0.11)	0.47 (0.25)	0.36 (0.22)
\mathbf{g}_{JL}	0.29 (0.21)	0.45 (0.25)	0.24 (0.17)	0.48 (0.27)	0.36 (0.25)
\mathbf{g}_L	0.28 (0.20)	0.14 (0.11)	0.19 (0.14)	0.21 (0.13)	0.23 (0.17)
\mathbf{g}_j	0.27 (0.20)	0.19 (0.16)	0.21 (0.15)	0.17 (0.16)	0.22 (0.18)
L	0.19 (0.14)	0.16 (0.12)	0.22 (0.14)	0.14 (0.12)	0.19 (0.15)

the most numerous (Table 3), the **p**-adjusted set works better than the **g**-adjusted set, helping to understand why the overlap score is bigger for **p**.

Following the same logic, we can estimate how well other vectors available during the dynamics would do for adjusting velocity after hopping. In addition to **p** and \mathbf{g}_{JL} , I considered the following **q** vectors: the nuclear velocity (**v**), the potential energy gradients of each state (\mathbf{g}_L and \mathbf{g}_j), and the angular momentum in relation to the center of mass (**L**). The mean value and standard deviation for the collection of P_{qh} values for all of these vectors are given in Table 5. **p**, **v**, and \mathbf{g}_{JL} have bigger projections over all types of hoppings (0.4 overall average), while \mathbf{g}_L , \mathbf{g}_j , and

L have the smallest (0.2 overall average). Thus, only the first three vectors should be considered for alternative velocity adjustment.

IV. CONCLUSIONS

Trajectory-independent surface hopping algorithms require velocity adjustment after hopping to enforce total energy conservation. Semiclassical analysis shows that this adjustment must be made in the direction of the nonadiabatic coupling vector \mathbf{h} . Nevertheless, the emergence of diverse surface hopping algorithms not requiring explicit \mathbf{h} calculations has led to the popularization of adjustment in alternative directions, the most common being the directions of either the linear momentum \mathbf{p} or velocity \mathbf{v} . In this paper, I benchmarked ethylene's nonadiabatic dynamics based on decoherence-corrected fewest-switches surface hopping, with velocity adjustment in \mathbf{h} , \mathbf{p} , and \mathbf{g} (gradient difference) vectors.

Ethylene was chosen for this benchmark due to its ultrafast and well-known nonadiabatic dynamics. Moreover, ethylene's intersection seam is a prototype for that of many larger organic molecules, ensuring some transferability of the conclusions. Given ethylene's small size, any effect of the velocity-adjustment direction must be amplified by the limited number of degrees of freedom. Thus, the results reported in this paper should be considered an upper limit of this effect on dynamics.

The results show that both the excited-state dynamics and the ground-state structural evolution are the same for all three approaches. Answering the question on whether the velocity-adjustment direction affects surface hopping dynamics, statistical analysis using an overlap score showed that for small trajectory ensembles (100 trajectories), the results are quantitatively equivalent within the margin of error for the 95% confidence level. For medium-sized ensembles (500 trajectories), \mathbf{p} -adjusted dynamics gives still acceptable results, while \mathbf{g} -adjusted already shows larger variations in relation to the \mathbf{h} -adjusted reference data. For large ensembles (> 1000 trajectories), both \mathbf{p} - and \mathbf{g} -adjusted sets show significant differences from the \mathbf{h} -adjusted set.

The reason for the relatively good performance of \mathbf{p} and, to a minor extent, \mathbf{g} directions is connected to how much these directions are parallel to \mathbf{h} at the hopping time. Beyond \mathbf{p} and \mathbf{g} , the nuclear velocity \mathbf{v} may also provide an appropriate direction for velocity adjustment. On the other hand, single-state gradients and angular momentum directions have too little projection on \mathbf{h} to be useful for adjustment.

This benchmark is limited to a single molecule and a single surface hopping variant. Given the prototypical role of ethylene and the successful adoption of DC-FSSH, the conclusions outlined above should be useful to inform on the maximum errors to expect when choosing a particular adjustment direction for surface hopping dynamics of other molecular systems. Moreover, I have defined clear protocols for the statistical analysis, including introducing the $\Lambda^{(1,2)}$ score to compare different data sets, and made all raw data readily available.⁴⁸ Thus, extensions of this benchmark toward other molecule types and methods may be seamlessly executed.

AUTHOR INFORMATION

Corresponding Author

Mario Barbatti – Aix Marseille University, CNRS, ICR, Marseille, France; orcid.org/0000-0001-9336-6607; Email: mario.barbatti@univ-amu.fr; www.barbatti.org

Complete contact information is available at: <https://pubs.acs.org/10.1021/acs.jctc.1c00012>

Notes

The author declares no competing financial interest.

ACKNOWLEDGMENTS

I am grateful for the support of the European Research Council (ERC) Advanced grant SubNano (Grant agreement 832237) and the project Equip@Meso (ANR-10-EQPX-29-01) funded by the French Government "Investissements d'Avenir" program for the computational resources.

REFERENCES

- (1) Nelson, T. R.; White, A. J.; Bjorggaard, J. A.; Sifain, A. E.; Zhang, Y.; Nebgen, B.; Fernandez-Alberti, S.; Mozyrsky, D.; Roitberg, A. E.; Tretiak, S. Non-adiabatic Excited-State Molecular Dynamics: Theory and Applications for Modeling Photophysics in Extended Molecular Materials. *Chem. Rev.* **2020**, *120*, 2215–2287.
- (2) Crespo-Otero, R.; Barbatti, M. Recent Advances and Perspectives on Nonadiabatic Mixed Quantum-Classical Dynamics. *Chem. Rev.* **2018**, *118*, 7026–7068.
- (3) Worth, G. A.; Cederbaum, L. S. Beyond Born-Oppenheimer: Molecular Dynamics through a Conical Intersection. *Annu. Rev. Phys. Chem.* **2004**, *55*, 127–158.
- (4) Tully, J. C. Molecular-Dynamics with Electronic-Transitions. *J. Chem. Phys.* **1990**, *93*, 1061–1071.
- (5) Herman, M. F. Nonadiabatic semiclassical scattering. I. Analysis of generalized surface hopping procedures. *J. Chem. Phys.* **1984**, *81*, 754–763.
- (6) Herman, M. F. A Semiclassical Surface Hopping Propagator for Nonadiabatic Problems. *J. Chem. Phys.* **1995**, *103*, 8081–8097.
- (7) Pechukas, P. Time-Dependent Semiclassical Scattering Theory. II. Atomic Collisions. *Phys. Rev.* **1969**, *181*, 174–185.
- (8) Coker, D. F.; Xiao, L. Methods for molecular dynamics with nonadiabatic transitions. *J. Chem. Phys.* **1995**, *102*, 496–510.
- (9) Hammes-Schiffer, S.; Tully, J. C. Proton-Transfer in Solution - Molecular-Dynamics with Quantum Transitions. *J. Chem. Phys.* **1994**, *101*, 4657–4667.
- (10) Tapavicza, E.; Tavernelli, I.; Rothlisberger, U. Trajectory Surface Hopping within Linear Response Time-Dependent Density-Functional Theory. *Phys. Rev. Lett.* **2007**, *98*, No. 023001.
- (11) Werner, U.; Mitrić, R.; Suzuki, T.; Bonačić-Koutecký, V. Nonadiabatic Dynamics within the Time Dependent Density Functional Theory: Ultrafast Photodynamics in Pyrazine. *Chem. Phys.* **2008**, *349*, 319–324.
- (12) Plasser, F.; Crespo-Otero, R.; Pederzoli, M.; Pittner, J.; Lischka, H.; Barbatti, M. Surface Hopping Dynamics with Correlated Single-Reference Methods: 9H-Adenine as a Case Study. *J. Chem. Theory Comput.* **2014**, *10*, 1395–1405.
- (13) Gao, X.; Bai, S.; Fazzi, D.; Niehaus, T.; Barbatti, M.; Thiel, W. Evaluation of Spin-Orbit Couplings with Linear-Response Time-Dependent Density Functional Methods. *J. Chem. Theory Comput.* **2017**, *13*, 515–524.
- (14) Granucci, G.; Persico, M.; Toniolo, A. Direct Semiclassical Simulation of Photochemical Processes with Semiempirical Wave Functions. *J. Chem. Phys.* **2001**, *114*, 10608–10615.
- (15) Plasser, F.; Granucci, G.; Pittner, J.; Barbatti, M.; Persico, M.; Lischka, H. Surface Hopping Dynamics Using a Locally Diabatic Formalism: Charge Transfer in the Ethylene Dimer Cation and Excited State Dynamics in the 2-Pyridone Dimer. *J. Chem. Phys.* **2012**, *137*, 22A514–13.
- (16) Zhu, C.; Nobusada, K.; Nakamura, H. New implementation of the trajectory surface hopping method with use of the Zhu–Nakamura theory. *J. Chem. Phys.* **2001**, *115*, 3031–3044.
- (17) Yu, L.; Xu, C.; Lei, Y.; Zhu, C.; Wen, Z. Trajectory-based nonadiabatic molecular dynamics without calculating nonadiabatic

- coupling in the avoided crossing case: trans \leftrightarrow cis photoisomerization in azobenzene. *Phys. Chem. Chem. Phys.* **2014**, *16*, 25883–25895.
- (18) Suchan, J.; Janos, J.; Slavicek, P. Pragmatic Approach to Photodynamics: Mixed Landau-Zener Surface Hopping with Intersystem Crossing. *J. Chem. Theory Comput.* **2020**, *16*, 5809–5820.
- (19) Belyaev, A. K.; Lasser, C.; Trigila, G. Landau–Zener Type Surface Hopping Algorithms. *J. Chem. Phys.* **2014**, *140*, No. 224108.
- (20) Xie, W.; Sapunar, M.; Došlić, N.; Sala, M.; Domcke, W. Assessing the performance of trajectory surface hopping methods: Ultrafast internal conversion in pyrazine. *J. Chem. Phys.* **2019**, *150*, No. 154119.
- (21) Shenai, P. M.; Fernandez-Alberti, S.; Bricker, W. P.; Tretiak, S.; Zhao, Y. Internal Conversion and Vibrational Energy Redistribution in Chlorophyll A. *J. Phys. Chem. B* **2016**, *120*, 49–58.
- (22) Alfonso-Hernandez, L.; Athanasopoulos, S.; Tretiak, S.; Miguel, B.; Bastida, A.; Fernandez-Alberti, S. Vibrational energy redistribution during donor–acceptor electronic energy transfer: criteria to identify subsets of active normal modes. *Phys. Chem. Chem. Phys.* **2020**, *22*, 18454–18466.
- (23) Soler, M. A.; Roitberg, A. E.; Nelson, T.; Tretiak, S.; Fernandez-Alberti, S. Analysis of State-Specific Vibrations Coupled to the Unidirectional Energy Transfer in Conjugated Dendrimers. *J. Phys. Chem. A* **2012**, *116*, 9802–9810.
- (24) Sellner, B.; Barbatti, M.; Lischka, H. Dynamics starting at a conical intersection: application to the photochemistry of pyrrole. *J. Chem. Phys.* **2009**, *131*, No. 024312.
- (25) Plasser, F.; Gómez, S.; Menger, M. F. S. J.; Mai, S.; González, L. Highly efficient surface hopping dynamics using a linear vibronic coupling model. *Phys. Chem. Chem. Phys.* **2019**, *21*, 57–69.
- (26) Ibele, L. M.; Curchod, B. F. E. A molecular perspective on Tully models for nonadiabatic dynamics. *Phys. Chem. Chem. Phys.* **2020**, *22*, 15183–15196.
- (27) Viel, A.; Krawczyk, R. P.; Manthe, U.; Domcke, W. Photoinduced dynamics of ethene in the N, V, and Z valence states: A six-dimensional nonadiabatic quantum dynamics investigation. *J. Chem. Phys.* **2004**, *120*, 11000–11010.
- (28) Zhou, W.; Mandal, A.; Huo, P. Quasi-Diabatic Scheme for Nonadiabatic On-the-Fly Simulations. *J. Phys. Chem. Lett.* **2019**, *10*, 7062–7070.
- (29) Ben-Nun, M.; Quenneville, J.; Martínez, T. J. Ab Initio Multiple Spawning: Photochemistry from First Principles Quantum Molecular Dynamics. *J. Phys. Chem. A* **2000**, *104*, 5161–5175.
- (30) Mori, T.; Glover, W. J.; Schuurman, M. S.; Martínez, T. J. Role of Rydberg States in the Photochemical Dynamics of Ethylene. *J. Phys. Chem. A* **2012**, *116*, 2808–2818.
- (31) Tao, H.; Allison, T. K.; Wright, T. W.; Stooke, A. M.; Khurmi, C.; van Tilborg, J.; Liu, Y.; Falcone, R. W.; Belkacem, A.; Martínez, T. J. Ultrafast internal conversion in ethylene. I. The excited state lifetime. *J. Chem. Phys.* **2011**, *134*, No. 244306.
- (32) Yu, J. K.; Bannwarth, C.; Hohenstein, E. G.; Martínez, T. J. Ab Initio Nonadiabatic Molecular Dynamics with Hole–Hole Tamm–Dancoff Approximated Density Functional Theory. *J. Chem. Theory Comput.* **2020**, *16*, 5499–5511.
- (33) Saita, K.; Shalashilin, D. V. On-the-fly ab initio molecular dynamics with multiconfigurational Ehrenfest method. *J. Chem. Phys.* **2012**, *137*, No. 22A506.
- (34) Barbatti, M.; Ruckebauer, M.; Lischka, H. The photodynamics of ethylene: a surface-hopping study on structural aspects. *J. Chem. Phys.* **2005**, *122*, No. 174307.
- (35) Barbatti, M.; Granucci, G.; Persico, M.; Lischka, H. Semiempirical molecular dynamics investigation of the excited state lifetime of ethylene. *Chem. Phys. Lett.* **2005**, *401*, 276–281.
- (36) Mališ, M.; Lubner, S. Trajectory Surface Hopping Nonadiabatic Molecular Dynamics with Kohn–Sham Δ SCF for Condensed-Phase Systems. *J. Chem. Theory Comput.* **2020**, *16*, 4071–4086.
- (37) Pradhan, E.; Sato, K.; Akimov, A. V. Non-adiabatic molecular dynamics with Δ SCF excited states. *J. Phys.: Condens. Matter* **2018**, *30*, No. 484002.
- (38) Hollas, D.; Šišťák, L.; Hohenstein, E. G.; Martínez, T. J.; Slavicek, P. Nonadiabatic Ab Initio Molecular Dynamics with the Floating Occupation Molecular Orbital-Complete Active Space Configuration Interaction Method. *J. Chem. Theory Comput.* **2018**, *14*, 339–350.
- (39) Sellner, B.; Barbatti, M.; Müller, T.; Domcke, W.; Lischka, H. Ultrafast Non-Adiabatic Dynamics of Ethylene Including Rydberg States. *Mol. Phys.* **2013**, *111*, 2439–2450.
- (40) Fischer, M.; Handt, J.; Schmidt, R. Nonadiabatic quantum molecular dynamics with hopping. III. Photoinduced excitation and relaxation of organic molecules. *Phys. Rev. A* **2014**, *90*, No. 012527.
- (41) Improta, R.; Santoro, F.; Blancafort, L. Quantum Mechanical Studies on the Photophysics and the Photochemistry of Nucleic Acids and Nucleobases. *Chem. Rev.* **2016**, *116*, 3540–3593.
- (42) Ditchfield, R.; Hehre, W. J.; Pople, J. A. Self-Consistent Molecular-Orbital Methods. IX. Extended Gaussian-Type Basis for Molecular-Orbital Studies of Organic Molecules. *J. Chem. Phys.* **1971**, *54*, 724–728.
- (43) Granucci, G.; Persico, M. Critical appraisal of the fewest switches algorithm for surface hopping. *J. Chem. Phys.* **2007**, *126*, No. 134114.
- (44) Lischka, H.; Shepard, R.; Müller, T.; Szalay, P. G.; Pitzer, R. M.; Aquino, A. J. A.; Araújo do Nascimento, M. M.; Barbatti, M.; Belcher, L. T.; Blaudeau, J.-P.; et al. The generality of the GUGA MRCI approach in COLUMBUS for treating complex quantum chemistry. *J. Chem. Phys.* **2020**, *152*, No. 134110.
- (45) Lischka, H.; Shepard, R.; Shavitt, I.; Pitzer, R. M.; Dallos, M.; Müller, T.; Szalay, P. G.; Brown, F. B.; Ahlrichs, R.; Böhm, H. J. et al. COLUMBUS, An Ab Initio Electronic Structure Program, Release 7.0. Available via the Internet at www.univie.ac.at/columbus, 2017.
- (46) Barbatti, M.; Granucci, G.; Ruckebauer, M.; Plasser, F.; Crespo-Otero, R.; Pittner, J.; Persico, M.; Lischka, H. NEWTON-X: A package for Newtonian Dynamics Close to the Crossing Seam (v. 2.2). Available via the Internet at www.newtonx.org, 2018.
- (47) Barbatti, M.; Ruckebauer, M.; Plasser, F.; Pittner, J.; Granucci, G.; Persico, M.; Lischka, H. Newton-X: a surface-hopping program for nonadiabatic molecular dynamics. *WIREs Comp. Mol. Sci.* **2014**, *4*, 26–33.
- (48) Barbatti, M. *Ethylene DC-FSSH: Momentum Adjustment. figshare. Dataset*, 2021.
- (49) Fabiano, E.; Keal, T. W.; Thiel, W. Implementation of Surface Hopping Molecular Dynamics Using Semiempirical Methods. *Chem. Phys.* **2008**, *349*, 334–347.
- (50) Weingart, O.; Nenov, A.; Altoè, P.; Rivalta, I.; Segarra-Martí, J.; Dokukina, I.; Garavelli, M. COBRAMM 2.0 — A software interface for tailoring molecular electronic structure calculations and running nanoscale (QM/MM) simulations. *J. Mol. Model.* **2018**, *24*, No. 271.
- (51) Polli, D.; Rivalta, I.; Nenov, A.; Weingart, O.; Garavelli, M.; Cerullo, G. Tracking the Primary Photoconversion Events in Rhodopsins by Ultrafast Optical Spectroscopy. *Photochem. Photobiol. Sci.* **2015**, *14*, 213–228.
- (52) Farmanara, P.; Steinkellner, O.; Wick, M. T.; Wittmann, M.; Korn, G.; Stert, V.; Radloff, W. Ultrafast internal conversion and photodissociation of molecules excited by femtosecond 155 nm laser pulses. *J. Chem. Phys.* **1999**, *111*, 6264–6270.
- (53) Farmanara, P.; Stert, V.; Radloff, W. Ultrafast internal conversion and fragmentation in electronically excited C₂H₄ and C₂H₃Cl molecules. *Chem. Phys. Lett.* **1998**, *288*, 518–522.
- (54) Mestdagh, J. M.; Visticot, J. P.; Elhanine, M.; Soep, B. Prereactive evolution of monoalkenes excited in the 6 eV region. *J. Chem. Phys.* **2000**, *113*, 237–248.
- (55) Stert, V.; Lippert, H.; Ritze, H. H.; Radloff, W. Femtosecond time-resolved dynamics of the electronically excited ethylene molecule. *Chem. Phys. Lett.* **2004**, *388*, 144–149.
- (56) Kosma, K.; Trushin, S. A.; Fuss, W.; Schmid, W. E. Ultrafast dynamics and coherent oscillations in ethylene and ethylene-d(4) excited at 162 nm. *J. Phys. Chem. A* **2008**, *112*, 7514–7529.
- (57) Kobayashi, T.; Horio, T.; Suzuki, T. Ultrafast Deactivation of the $\pi\pi^*$ (V) State of Ethylene Studied Using Sub-20 fs Time-Resolved Photoelectron Imaging. *J. Phys. Chem. A* **2015**, *119*, 9518–9523.
- (58) Yarkony, D. R. Nuclear dynamics near conical intersections in the adiabatic representation. I. The effects of local topography on interstate transitions. *J. Chem. Phys.* **2001**, *114*, 2601–2613.